atmosphere

MDPI

Article

Cloud Characteristics during Intense Cold Air Outbreaks over the Barents Sea Based on Satellite Data

Alexandra Narizhnaya [1,*] and Alexander Chernokulsky [1,2]

[1] A. M. Obukhov Institute of Atmospheric Physics, Russian Academy of Sciences, Pyzhevsky 3, 119017 Moscow, Russia; a.chernokulsky@ifaran.ru
[2] Institute of Geography, Russian Academy of Sciences, Staromonetny 29, 119017 Moscow, Russia
* Correspondence: alex.narizhnaya@ifaran.ru

Abstract: The Arctic experiences remarkable changes in environmental parameters that affect fluctuations in the surface energy budget, including radiation and sensible and latent heat fluxes. Cold air masses and cloud transformations during marine cold air outbreaks (MCAOs) substantially influence the radiative fluxes, thereby shaping the link between large-scale dynamics, sea ice conditions, and the surface energy budget. In this study, we investigate various cloud characteristics during intense MCAOs over the Barents Sea from 2000 to 2018 using satellite data. We identify 72 intense MCAO events that propagated southward using reanalysis data of the surface temperature and potential temperature at the 800 hPa level. We investigate the macro- and microphysical parameters and radiative properties of clouds within selected MCAOs, their dependence on sea ice concentration, and their initial air mass properties using satellite data. A significant increase in low-level clouds near the ice edge (up to +25% anomalies) and a smooth transition to upper-level clouds is revealed. The total cloud top height during intense MCAOs is generally 500–700 m lower than under neutral conditions. MCAOs induce a positive net cloud radiative effect, which peaks at +20 W m^{-2} (100 km from the ice edge) and gradually decreases towards the continent (−2.3 W m^{-2} per 100 km). Our study provides evidence for the importance of changes in the cloud radiative effect within MCAOs, which should be accurately simulated in regional and global climate models.

Keywords: cold air outbreak; cloud radiative characteristics; arctic climate; Barents Sea; air–sea interaction; environmental satellite

Citation: Narizhnaya, A.; Chernokulsky, A. Cloud Characteristics during Intense Cold Air Outbreaks over the Barents Sea Based on Satellite Data. *Atmosphere* **2024**, *15*, 317. https://doi.org/10.3390/atmos15030317

Academic Editor: Filomena Romano

Received: 4 January 2024
Revised: 24 February 2024
Accepted: 25 February 2024
Published: 2 March 2024

1. Introduction

In recent decades, the Arctic regions have been warming two to three times faster than the planet as a whole [1,2]. Temperature changes are accompanied by reductions in sea ice area and thickness [3,4], increases in air humidity [5], changes in cloud cover [6–8], and changes in circulation regimes [3,9]. Changes in the characteristics of marine cold air outbreaks (MCAOs) over the Arctic Ocean are particularly indicative of circulation changes [5,10], which are critical for atmospheric interactions between the Arctic and mid-latitudes [11]. In the Arctic, MCAOs occur when relatively cold and dry air masses from the sea ice regions move over the comparatively warmer ocean surface, triggering turbulent heat and moisture fluxes and promoting cloud formation [12–14]. One of the main regions for MCAO formation is the area of the Barents Sea, where MCAOs are most likely to occur during the southward flow from the polar regions north of Franz Josef Land or Svalbard over into the Barents Sea (BS) Basin [13,15–17]. Although MCAOs occur throughout the year, they are most severe during the cold season when the sea–air temperature contrast is greatest [12,17,18]. On average, MCAOs develop and dissipate over several hours to several days [19,20] and can extend over 1000 km in severe cases [13,21] in the rear of midlatitude lows. A poleward shift in the tracks of these lows [22] fosters changes in MCAOs frequency and intensity [10].

MCAOs crucially affect the ocean–atmosphere heat exchange, and cloud dynamics strongly influence this exchange. In that regard, in Ref. [18], it was shown that MCAOs are responsible for 60–80% of the oceanic heat loss in the northern seas. MCAOs are characterized by anomalously high values of sensible and latent heat fluxes, reaching up to 200–700 W m^{-2} [12,16] or even exceeding 700 W m^{-2} [23,24]. Radiation fluxes and hence, the surface radiative budget (SRB), are strongly affected by cloud dynamics within MCAOs [14]. Clouds obtain a specific structure under conditions of intense heat transfer and enhanced convection in the surface layer of the atmosphere during MCAO development [13,14,25,26]. More specifically, the so-called stratocumulus-to-cumulus transformation of the cloud cover in the MCAO is usually considered (e.g., [15,21,27,28]).

Despite its importance, the dynamics of radiative fluxes during MCAOs and their association with clouds is relatively understudied compared to sensible and latent heat fluxes. Estimates of the radiative properties of cloud during MCAOs are rather scarce. In particular, ground-based studies are limited by a small number of expeditionary campaigns (e.g., COMBLE, ACTIVATE, EarthCARE, etc.), while model experiments are not yet perfect at reproducing MCAOs (e.g., [29,30]) and cannot yet provide a reliable and complete picture of the transformation of cloud influence on radiation effects within MCAO development. Several studies have examined clouds within MCAOs using satellite data [23,27,31–33], focusing mainly on changes in macrophysical cloud characteristics within MCAOs, including their behavior with respect to proximity to the ice edge. However, little is known about changes in the radiative properties of clouds, i.e., the cloud radiative effect, within MCAOs. In addition, a number of research studies are devoted to clouds within MCAOs in the North Atlantic region, while less is known about cloud parameters within MCAOs over the Barents Sea, which is recognized as one of the key regions of Arctic influence on mid-latitude weather regimes [34].

In this study, we focus on the cloud radiative characteristics of the atmosphere during intense cold air outbreaks over the Barents Sea using CERES satellite data for the period of 2000–2018. In particular, we evaluate the absolute and anomaly values of various cloud and radiation characteristics of intense MCAOs over the Barents Sea, as well as their transformation within the MCAO. We also evaluate how the cloud radiative characteristics of such untense MCAOs change with respect to various background conditions such as air mass and sea surface temperature. In Section 2, we specify the research area and describe the data and methods used, in Section 3 we present the main results, and in Section 4, we summarize the results and suggest future work motivated by this study.

2. Materials and Methods

2.1. Study Area

Our analysis focuses on the intense MCAOs that formed within deep lows that penetrated from the Atlantic to the Arctic and developed primarily over the Barents Sea. Figure 1 shows an example of such a low (Figure 1a) and the cloud cover (Figure 1b) within an MCAO that formed in the rear part of this area. In particular, the distinct transformation of stratiform cloud streets into broken open or closed cells downstream can be observed.

The study area covers the BS and its surrounding areas (Figure 2). Within this region, we selected several subregions to define and describe MCAO characteristics. In this study, we focused on intense MCAOs moving southward from the polar ice caps, from the sea ice edge. We defined the severity of MCAOs using the M-index (see Section 2.3.1 for more details), based on information from the region in the southern BS (67–73° N and 30–50° E, see box #2 in Figure 2); specifically, the average of the M-index in this area should be $\geq$3 K. The formation of the most intense MCAOs in the BS region most often occurs under conditions of strong northerly winds [13,18]. Therefore, the central part of the BS (73–77° N and 30–50° E, see box #1 in Figure 2), adjacent to the climatological sea ice edge, was used for the selection of such outbreaks by checking the wind conditions (see Section 2.3.1).

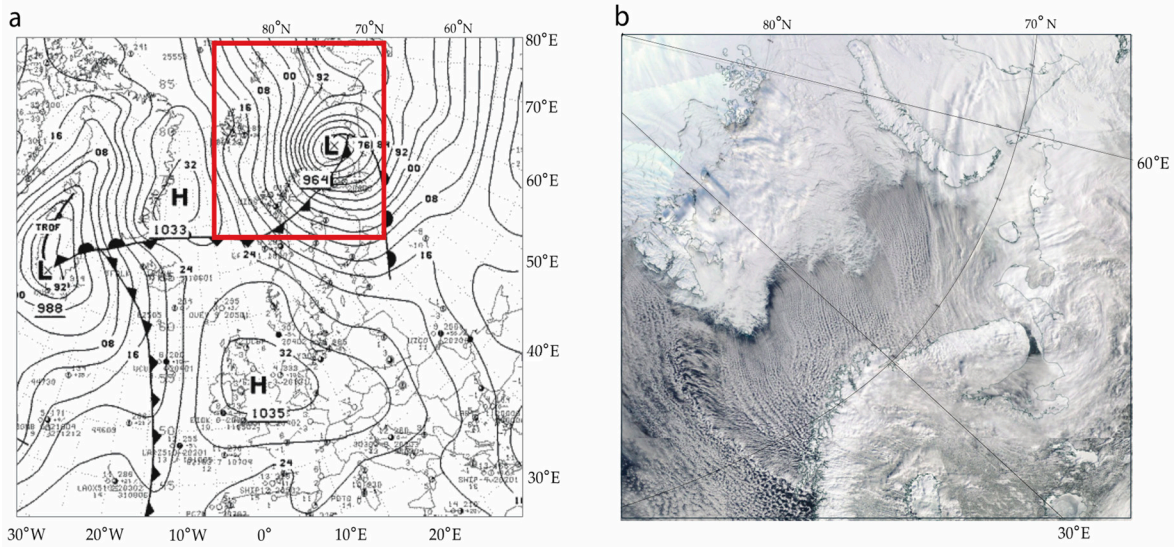

Figure 1. An example of a marine cold air outbreak on 19 March 2003: (**a**) the surface analysis map at 03:00 UTC retrieved from Ref. [35] (the red frame outlines the area shown in the satellite image in (**b**)); (**b**) cloud cover over the Barents Sea on 19 March 2003 (around 10:00 UTC) obtained from NASA Worldview (based on the Terra/Aqua MODIS satellite images [36]).

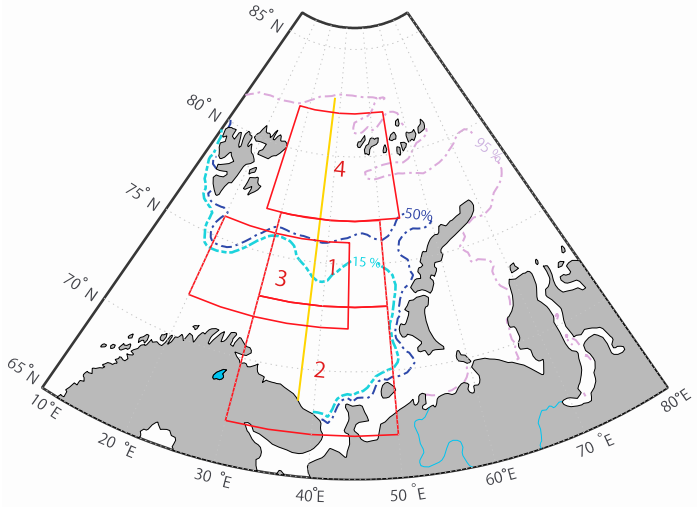

Figure 2. Analysis region (65–86° N, 10–80 ° E) and areas used for sample selection or specific analysis for MCAO: in box #1, the wind condition is obtained; in box #2, MCAO severity is noted, and the sea surface temperature is calculated; box #3 is used for averaging cloud radiative characteristics for further composite analysis; box #4 is used for averaging the moisture content of the intruding air masses. Dotted lines show mean sea ice concentration values at 15%, 50%, and 95% (data from NSIDC archive [37,38]), averaged over the analyzed sample of intense MCAOs. The orange line shows the section of the 38th meridian extending south of the 95% sea ice edge position for the analysis of the composite profiles of the cloud radiative parameters.

We investigated the cloud radiative properties of MCAOs over the BS and surrounding areas and their dependence on climatic parameters, including sea ice extent in the Barents Sea, sea surface temperature (SST), and moisture content of the incoming air mass. The area in the northern part of the BS (77–82° N, 27–54° E, box #4 in Figure 2) was used to calculate the moisture content of the incoming air masses. For the SST calculation, the region in the south of the Barents Sea (box #2 in Figure 2) was used. The cloud characteristics were calculated for the entire region, but also averaged over the central ice-free region of the BS (72–76° N, 20–44° E, box #3 in Figure 2). Box #3 is defined as the area where the largest anomalies in cloud characteristics are observed during intense MCAOs (see Section 3). We

also analyzed changes in cloud characteristics accompanying the MCAO propagation from the sea ice edge. We chose the 38 °E meridian for this analysis to capture the central basin of the BS, as well as to maximize the length of the open water area, given the 95% sea ice edge position to the north and the continental coast to the south.

2.2. Data

2.2.1. Reanalysis Data

As the main data source for MCAO identification, we used the 6 h ERA-Interim reanalysis data for the surface and air temperature and pressure from January 2000 to January 2018, with a resolution of 0.75° × 0.75° [39]. Since MCAO events typically last several hours and cover a relatively large area [40], we assume that the spatial and temporal resolution available in the ERA-Interim reanalysis is sufficient to successfully identify such events, as was shown to be the case in many previous studies (see e.g., [17,21,40,41]). In Ref. [42], it was shown that the ERA-Interim reanalysis quite adequately reproduces the different characteristics of the Arctic atmosphere when compared to the observational data. We have also used ERA-Interim data to analyze the initial characteristics of the intruding air masses and the sea surface temperature of the BS.

2.2.2. Satellite Data

To analyze the cloud radiative characteristics, we used the Clouds and the Earth's Radiant Energy System (CERES) satellite data [43–45]. CERES measurements aim to assess the impact of clouds on the Earth's energy balance, which is one of the largest sources of uncertainty, and to produce time series of climate data from the Earth's radiation balance. The program has been monitoring clouds and radiation for more than 20 years, and includes measurements from the Terra and Aqua satellites. In particular, we used the CERES SYN1deg Ed4A product for the period of 2000–2018 [46,47]—this archive represents data regarding cloud properties and radiation fluxes on a regular grid, with a spatial resolution of 1° × 1° and an hourly time resolution. This product shows relatively good agreement with in situ cloud and radiation observations from the Arctic, especially over the open water regions [48], while over the sea ice, both shortwave and longwave fluxes are somewhat biased due to albedo and saturation effects [49]. In our study, we focus mainly on the ice-free regions over the central part of the BS, where we can rely on CERES remote sensing data.

Parameters such as cloud fraction (for low and total cloud cover), cloud height, cloud phase composition, pressure at the lower boundary of the cloud cover, cloud water content, and optical cloud thickness were analyzed. The cloud radiative effect was also calculated from the longwave and shortwave radiative fluxes as the difference between the fluxes under all-sky and clear-sky conditions [50]—see calculation details in Section 2.3.2. CERES provides calculated fluxes for clear sky conditions using a specific algorithm [43,46,51,52]. Therefore, we used the available products for the downward and upward longwave and shortwave radiation near the Earth's surface.

For additional analysis of several intense intrusions, cloud radiation characteristics were also obtained from MODIS (Moderate Resolution Imaging Spectroradiometer) data installed on the US Terra and Aqua polar-orbiting satellites. The second level of data (level 2), with a resolution of 5 km per pixel, was used, which is known to be sufficient to identify convective ridges and cells [27]. In particular, the so-called MOD06 and MYD06 products (for Terra and Aqua, respectively) were used [53]. Information on satellite pass times was obtained using satellite imagery and satellite orbit trajectories from NASA data [36,54].

In addition, we used satellite microwave observations to estimate the sea ice concentration (SIC), using the NSIDC Bootstrap version 3 product [38], which provides daily SIC data on a 25 km by 25 km polar stereographic grid. This dataset is presented for the polar region on a 25 km × 25 km polar stereographic grid, and daily values are available from 1978 to 2022.

2.3. Methods

2.3.1. MCAO Identification and Sampling

In this study, we identified the MCAO events and checked their severity using the M-index, K [55], which is defined as the difference in the vertical potential temperature between the ground (sea) surface and the mid-tropospheric layer:

$$M = \theta_{skt} - \theta_{800} \quad (1)$$

where θ_{skt} is the potential surface temperature, defined as $\theta_{skt} = T_{skt}\left(\frac{P_0}{P_{msl}}\right)^{R/c_p}$, $R/c_p = 0.288$, T_{skt} is the surface temperature, P_0 = 1000 hPa, and P_{msl} is the pressure above sea level; θ_{800} is the potential temperature at the level of 800 hPa.

In general, index M can be considered as a simple parameter of atmospheric stability. It was developed to determine the advection of cold air over the open ocean, which is warm relative to the air mass [16]. Various levels have been proposed for the calculation of the potential temperature of the mid-tropospheric layer, i.e., from 700 hPa [16,55]. However, the use of a surface at 800 hPa was found to better reproduce the MCAO characteristics at high latitudes [56].

The MCAO events were defined as contiguous oceanic areas meeting the criteria of M > 0 K in a grid cell (Figure 3a) [56]. We define the area of a certain MCAO intensity according to the mean M-index value in the cells within a group of at least eight adjacent cells to non-negative M-index cells (Figure 3b). The same number of ERA-Interim cells was previously considered (see, e.g., [56]) as sufficient to capture the onset of MCAO formation. In total, we identified 8108 6 h periods exhibiting MCAOs for 2000–2018 over the BS.

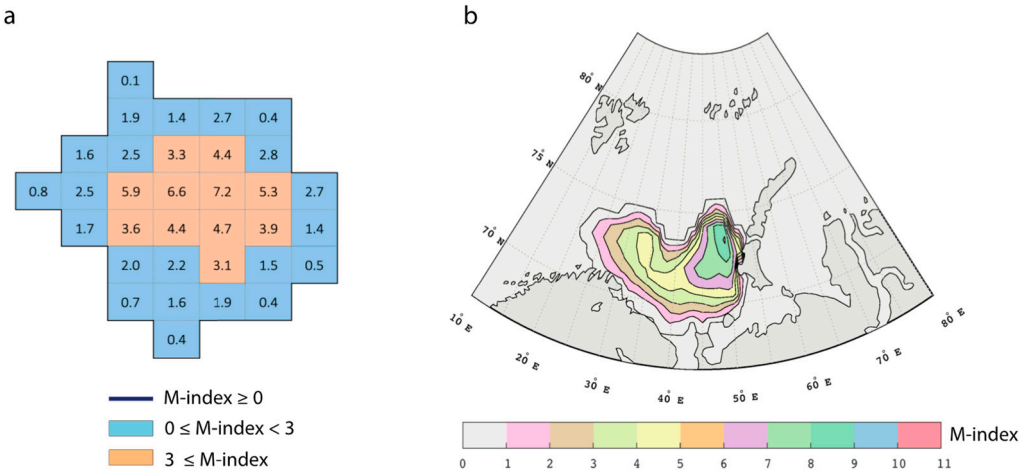

Figure 3. (**a**) Schematic example of the grid cell structure of an MCAO; (**b**) a distribution of the M-index within an example of an intense MCAO case for 19 March 2003, 12:00 UTC (the same case as that used in Figure 1).

For further analysis of cloud-radiation characteristics, based on satellite data for the period 2000–2018, a narrower sample of only intense MCAO cases was selected, i.e., those events with an M-index above 3 K averaged over the area indicated in box #2 (see Figure 2). The presence of the northern quarter strong wind in the area shown in box #1 (with a direction of from 335° to 25° and a windspeed > 3 m s^{-1}), i.e., wind from the sea ice edge, was an additional necessary condition for the MCAO event to fit the final sample. As a result, we selected 72 intense MCAO events that met these criteria. Using this approach, we conduct the analysis of MCAOs that were intensive enough to have reached the southern BS in the area shown in box #2, and which were specifically driven by the northerly advection of an Arctic air mass from the sea ice region. Although MCAOs during all seasons were initially examined, the winter season tends to dominate the final sample of intense MCAOs.

This sample consisted only of Arctic cold season MCAOs covering the months of November to April, whereas the majority of MCAOs occurred in winter (54 out of 72 cases).

2.3.2. Cloud Radiative Characteristics

We analyzed various cloud radiative characteristics for MCAOs. The list of variables is presented in Table 1.

Table 1. The list of analyzed cloud radiative characteristics. Note that the cloud characteristics are evaluated for total and low-level clouds, which are further denoted by the subscripts 'tot' and 'low', respectively. The low-level clouds in the CERES data refer to the layer from the surface to 700 hPa.

Parameter	Full Name	Unit
$CRE_{LW/SW/NET}$	Cloud radiative effect	W m^{-2}
$SRB_{LW/SW/NET}$	Surface radiative budget	W m^{-2}
N	Cloud fraction	%
COT	Cloud optical thickness	units
CTH	Cloud top height	km
LWP	Liquid water path	g m^{-2}
CBP	Cloud base pressure	hPa
CTP	Cloud top pressure	hPa
CPP	Cloud particle phase (1—liquid, 2—solid)	units
CTT	Cloud top temperature	K
IWV	Integral water vapor content	kg m^{-2}
EfR	Cloud droplet effective radius	µm

To calculate the impact of cloudiness on radiative fluxes during marine cold air outbreaks, we employed a well-known cloud radiative effect (CRE) approach (following, e.g., [50,57–60]), expressed as the difference in total radiative fluxes between natural atmospheric conditions (so called "all-sky conditions", AS) and clear-sky conditions (CS). The total cloud radiative effect at the surface (CRE_{NET}) is calculated as the sum of the shortwave (CRE_{SW}) and longwave (CRE_{LW}) cloud radiative effects:

$$CRE_{NET} = CRE_{SW} + CRE_{LW} \quad (2)$$

which are, respectively, described as follows:

$$CRE_{SW} = (SW\downarrow_{AS} - SW\uparrow_{AS}) - (SW\downarrow_{CS} - SW\uparrow_{CS}) \quad (3)$$

$$CRE_{LW} = (LW\downarrow_{AS} - LW\uparrow_{AS}) - (LW\downarrow_{CS} - LW\uparrow_{CS}) \quad (4)$$

where $SW\downarrow_{AS}$ and $LW\downarrow_{AS}$ are the downward shortwave and longwave radiation fluxes in the normal atmosphere, and $SW\downarrow_{CS}$ and $LW\downarrow_{CS}$ are the fluxes under cloud-free conditions. The positive CRE implies the warming effect of clouds compared to conditions under the cloudless atmosphere, while the cooling effect of clouds is represented by the negative values of the CRE.

2.3.3. Composite Analysis of Cloud Radiative Characteristics

Given the selected sample of 72 intense MCAO events, we constructed composite maps of the absolute values of cloud and radiation characteristics for the BS and neighboring regions based on CERES satellite data. The anomalies of the cloud characteristics were also estimated. These anomalies were calculated as the difference between the means for 72 selected MCAO cases and the means for the same time of day on the same calendar days as for these MCAOs, but for all 19 years from 2000 to 2018. The statistical significance of the anomalies was assessed using a Student's *t*-test (at the 95% level).

For the selected sample of 72 intense MCAO events, we also plotted composite profiles of changes in cloud and radiation characteristics along 38 °E (the orange line in Figure 2)

from the sea ice edge, defined as the 95% sea ice concentration. The sea ice edge was chosen as the starting point for each MCAO, while the ending point was the 800 km distance from this edge, which was usually sufficient to remain above the sea surface. For each profile, the mean of all selected MCAO events, the median, the 5th, 15th, 25th, 75th, and 95th percentiles were determined, and the linear trend coefficients were also calculated.

In addition, we analyzed the fine structure of clouds within the MCAOs using MODIS data with a 5 min temporal resolution. From a sample of 72 intense MCAO episodes, we identified the subsample of intense MCAOs when the Terra/Aqua satellites were directly over the BS region. In total, 19 such episodes were obtained for the Terra satellite and 14 for the Aqua satellite. Composite maps of cloud characteristics (cloud fraction, temperature, and pressure at the top of the cloud; effective radius; optical thickness; and cloud height) were then produced for the region with the maximum number of passes for each satellite.

2.3.4. Dependence of MCAO Cloud Characteristics on the Background Conditions

The scenarios for MCAO development are diverse and depend on background conditions, i.e., the characteristics of the air mass (e.g., lapse rate, humidity, etc.) and the underlying surface (e.g., sea ice edge position and sea surface temperature). In this study, we investigate the linkage of cloud characteristics within intense MCAOs over the BS with several background parameters, including the vertical integral water vapor content (IWV) of the intruding air mass, the sea surface temperature (SST), and the distance along the 38°E meridian from the sea ice edge (the 95% sea ice concentration boundary) to the Kola Peninsula. We used ERA-Interim reanalysis data for IWV and SST and NSIDC satellite data for sea ice (see Section 2.1 for information on the boxes in which the averaging is performed).

To estimate the dependence of cloud characteristics on the background conditions for the sample of intense MCAOs, non-parametric Theil–Sen slope estimators were calculated and their significance assessed using the Mann–Kendall test [61]. These slope estimators were calculated for each pair of cloud characteristics and background condition parameters. In addition, bootstrap-based 90% confidence intervals were assessed for each Theil–Sen slope estimator.

3. Results

3.1. Spatial Distribution of Cloud Characteristics for Intense MCAOs

The cloud cover in the MCAO is transformed as the air mass moves along the MCAO flow. As a result, both the micro- and macrophysical characteristics of the clouds and the radiative parameters change as well. We found a decrease in N_{low} (%) over the open water, which is explained by the transformation of the cloud structure, i.e., the transition from closed to open cells (Figure 4a). At the same time, the height of the low-level clouds increases (Figure 4b), the phase changes from ice crystals above the ice surface to an almost entirely liquid phase (Figure 4c), and the average values of the COT_{tot} increase from ~2.3 over ice to ~7.2 when moving to an open water surface (Figure 4d). The observed increase in the height of the lower cloud base is in good agreement with previous studies investigating the height of the planetary boundary layer (PBL) in MCAOs (see, e.g., [9,13,31]). The decrease in atmospheric pressure at the cloud base (Figure 4e), i.e., the increase in the cloud base height, is characteristic of the growth of the convective mixed layer, which is caused by temperature contrasts between the underlying relatively warm water surface and the cold air. The pressure drops from 980–880 hPa near the sea ice margin to ~820 hPa near the coastline.

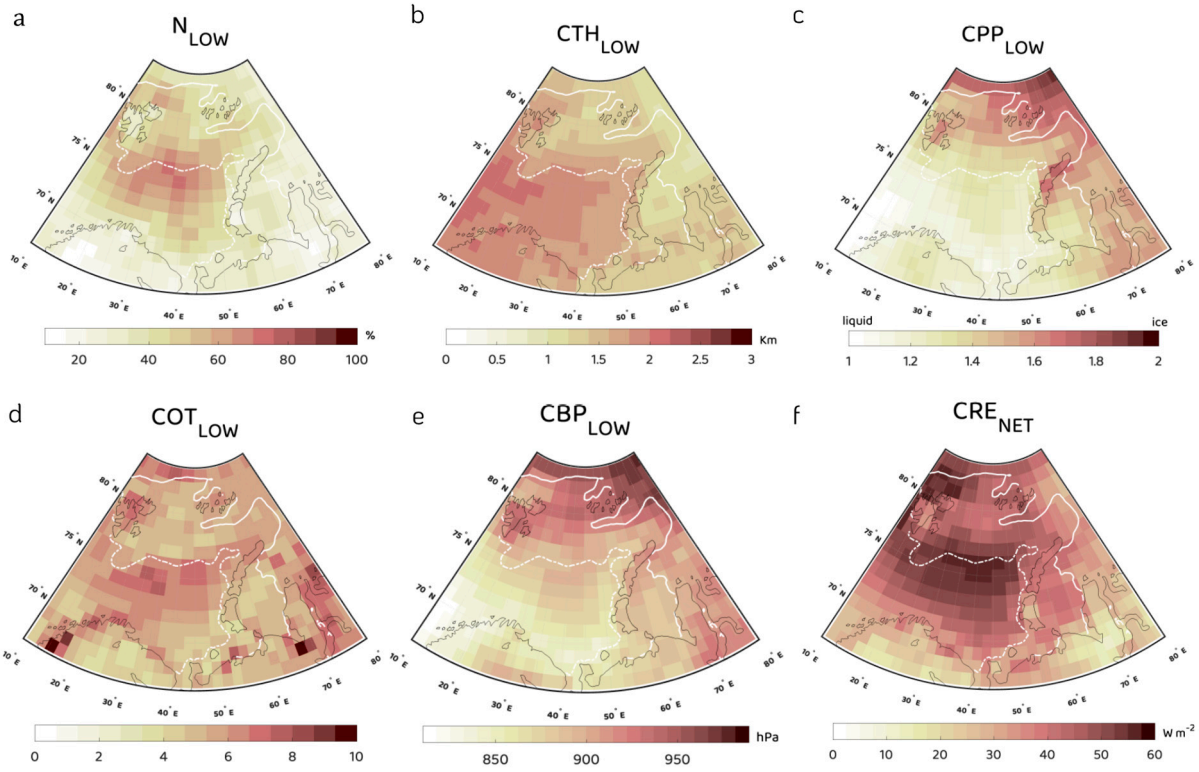

Figure 4. Composite maps of absolute values of several cloud characteristics for 72 intense MCAO events: (**a**) low-level cloud fraction (%); (**b**) low-level cloud top height (km); (**c**) cloud particle phase for low-level clouds (where 1 is liquid and 2 is ice); (**d**) low-level cloud optical depth; (**e**) low-level cloud base pressure (hPa); (**f**) net cloud radiative effect (W m^{-2}). The solid and dashed lines mark the position of the 95% and 30% ice concentration boundaries, respectively, averaged for the sample of the 72 analyzed MCAO episodes.

A strong increase in descending longwave radiation is found, with the absolute flux values reaching 300 W m^{-2} when the MCAO crosses the sea ice margin (Figure S1a). During the cold season, especially during the polar night, the LW fluxes provide the greatest contribution to the CRE_{NET}, which is why the values of the CRE_{LW} (Figure S1b) are similar to those of the CRE_{NET}. As the ice edge is approached, the absolute values of the CRE_{NET} increase sharply (from 38 W m^{-2} to 57 W m^{-2}, Figure 4f). Over open water, the warming effect of the clouds decreases (from 57 W m^{-2} to 45 W m^{-2} on average, Figure 4f), which is related to the transition of the clouds from closed to open cells [23,27,56].

Analysis of the composite maps of cloud radiative anomalies allows for the identification of features characteristic of a selected sample of intense MCAOs during the cold season over the Barents Sea. A significant increase in total cloudiness of 5–13%, compared to average conditions, was observed over the central basin of the Barents Sea during the MCAO periods (Figure 5b), along with an increase of 20–23% for low-level cloudiness during these periods (Figure 5a). In the lower, unstable stratified layer, the cloud particle phase shifts towards the liquid phase (Figure 5c). This leads to an increase in the liquid water path for both low-level and total clouds. For example, for the low-level clouds, the LWP anomaly varies from 15–20 g m^{-2} near the ice margin to more than 100 g/m^{-2} near the Kola Peninsula coast (Figure 5f). Larger LWP anomalies over land are not significant and may be due to uncertainties in LWP retrievals over the snow surface under conditions of a high solar zenith angle [48]. Positive low-level cloud base pressure anomalies (Figure 5e) indicate that clouds are lower during intense MCAOs compared to during average conditions. The total cloud top height decreases during intense MCAO conditions (Figure 5d), because all levels are considered for the total clouds, and the decrease in the high- and mid-level cloud fraction during MCAOs leads directly to the decrease in the cloud top height. At the

same time, the low-level cloud top height shows positive anomalies during MCAOs with respect to background conditions (Table 2) due to the development of convection [17,21]. Small variations were found in the low-level cloud top height during MCAOs, but these suggested a small decrease in this height for particularly strong MCAOs, while the causes of this decrease remain unclear and deserve further investigation.

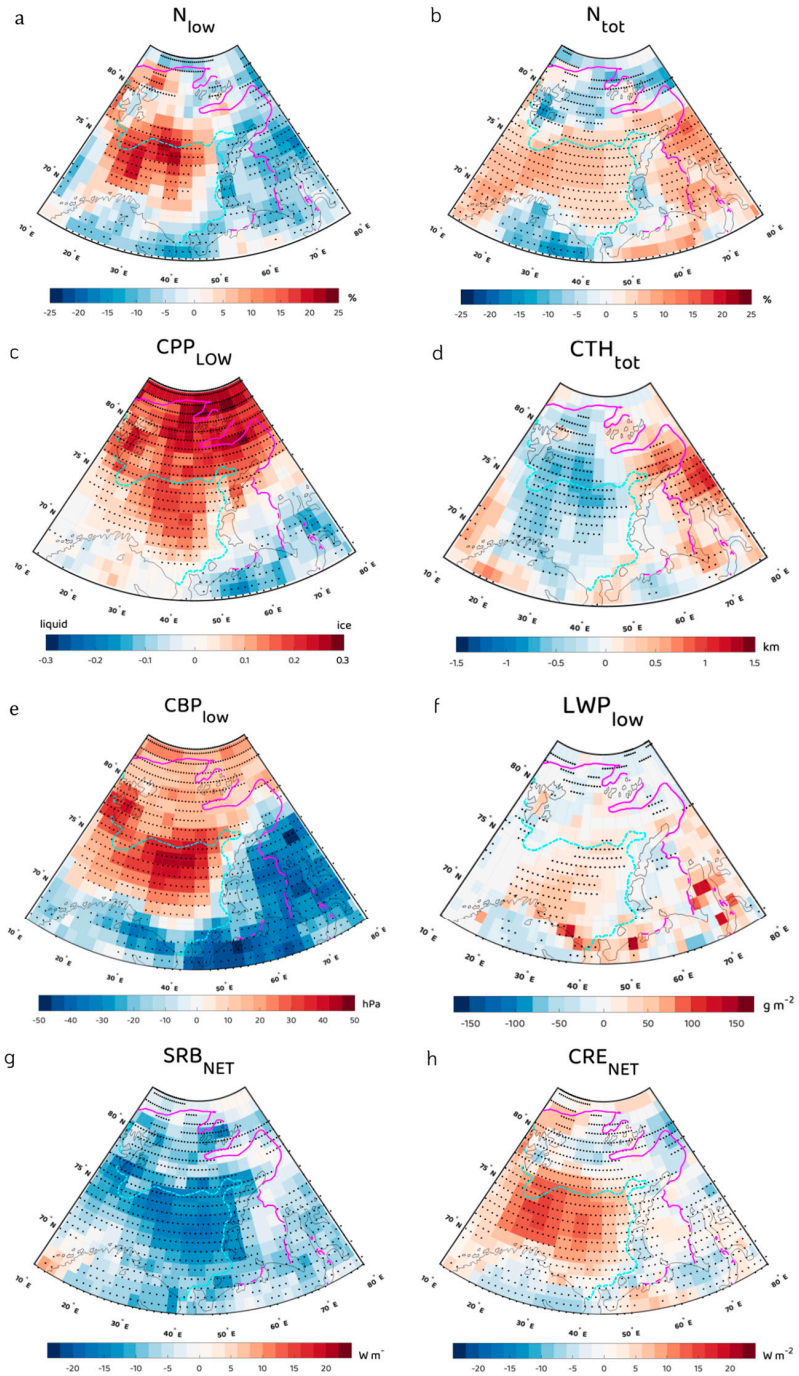

Figure 5. Composite maps of anomaly values of various cloud and radiation characteristics for 72 intense MCAO events: (**a**) low-level cloud fraction (%), (**b**) total cloud fraction (%), (**c**) low-level cloud particle phase (where 1 is liquid and 2 is ice), (**d**) total cloud top height (km), (**e**) low-level cloud base pressure (hPa), (**f**) low-level cloud liquid water path (g m^{-2}), (**g**) net surface radiation balance (W m^{-2}), and (**h**) net cloud radiative effect on the surface (W/m^2). The solid and dashed lines mark the position of the 95% and 30% ice concentration boundaries, respectively, averaged for the sample of the 72 analyzed MCAO episodes. Dots indicate significant anomalies at the 0.05 significance level.

Table 2. The absolute and anomaly values of selected parameters, averaged over the central region of the Barents Sea (box #3 in Figure 2).

Parameter	N_{tot}	N_{low}	CTH_{tot}	CTH_{low}	LWP_{tot}	LWP_{low}	COT_{tot}	COT_{low}	CBP_{tot}	CPP_{tot}	CPP_{low}	SRB_{LW}	CRE_{LW}	SRB_{SW}	CRE_{SW}	SRB_{NET}	CRE_{NET}
Units [1]	%	%	km	km	g/m^2	g/m^2	*	*	hPa	*	*	W/m^2	W/m^2	W/m^2	W/m^2	W/m^2	W/m^2
Absolute values	97.9	62.6	3.5	1.8	89.3	87.6	5.3	6.4	882.3	1.5	1.3	−67.6	70.1	13.8	−17.0	−53.8	53.1
Anomalies	6.7	15.9	−0.5	0.8	16.4	18.3	0.7	0.9	33.1	0.02	0.1	−13.8	13.1	0.1	−0.9	−13.7	12.2

[1] Unitless variables are indicated by an asterisk (*).

Clouds have a warming effect on the near-surface air layer over the open sea surface during the winter months [62,63]. In the case of intense MCAOs, the clouds become optically thicker and obtain a higher water content, which determines the positive anomalies of the CRE_{LW} up to 20–25 W m^{-2} (Figure S2). The positive anomalies indicate a stronger warming effect of clouds during MCAOs compared to under normal conditions. The values of the CRE_{NET} and SRB_{NET} anomalies during intense MCAOs are mainly determined by the anomalies of the LW effect. This results in positive CRE_{NET} anomalies of up to +20 W m^{-2} (Figure 5h) and negative SRB_{NET} anomalies of up to −18 W m^{-2} (Figure 5g).

The absolute and anomaly values of the cloud characteristics within intense MCAOs averaged over the central basin of the Barents Sea are presented in Table 2.

3.2. Changes in the Cloud Characteristics with MCAO Propagation

As mentioned above, clouds within MCAOs undergo a certain transformation as they move from the ice margin over open water. With the growth of the convectively unstable layer in the atmosphere, there is a decrease in N_{low} of 4%/100 km (Figure 6a), while the cloud top height increases from 3 km at the ice margin to 3.5 km at a distance of 800 km (Figure 6g). At the same time, there is a gradual decrease in cloud base pressure, with a trend of −4.9 hPa/100 km (Figure 6h). Low-level clouds begin to contain more liquid particles (Figure 6e), while in contrast, clouds of all layers tend to contain more ice crystals (Figure 6f). Moving away from the ice margin, clouds become optically thicker (Figure 6c,d), with a peak in COT at ~300 km from the ice margin (~7 for low-level clouds), after which a gradual decrease in COT is observed for both low-level and all clouds up to the continent, which is most likely a consequence of the stratocumulus-to-cumulus transition. The liquid water path gradually increases by 12.1 g m^{-2} for low-level clouds (Figure 6i) and by 12.7 g m^{-2} for all clouds (Figure S3a), reaching ~100 g m^{-2} and ~60 g m^{-2} near the continental boundary, respectively. For the radiative flux changes, the contribution of the LW flux changes is the most important. Due to the changes in the CRE_{LW} (Figure S3b), the values of the CRE_{NET} also change, gradually decreasing at a rate of −2.3 W m^{-2} per 100 km from its maximum around ~50–70 W m^{-2} near the ice margin to ~40–60 W m^{-2} closer to the continent.

3.3. Analysis of the Fine Structure of Cloud Characteristics within MCAOs Based on MODIS Data

The CERES-SYN data analyzed in the previous sections provide global coverage, with a spatial resolution of 1 degree and a temporal resolution of 1 h. The cloud data are based on the MODIS instrument installed on the polar-orbiting Terra/Aqua satellites, which fly over a given region at various time intervals. Therefore, data interpolation for times when the satellite is far from the study area is likely to be inaccurate and may introduce some errors into the cloud characteristics analyzed. To complement the above, we included the satellite data obtained directly at the time the satellite passed over the study area. These data were obtained directly from MODIS data (Level 2 data, MOD06_L2 and MYD06_L2 products) with a resolution of 5 min over a relatively small area for 33 MCAO events, including 19 and 14 events observed from the Terra and Aqua satellites, respectively (see

Section 2.2.2 for the details). Figure 7 shows the cloud characteristics averaged from the 19 events observed with the MODIS Terra instrument, while similar distributions are found for the 14 events observed using the MODIS Aqua satellite (Figure S4).

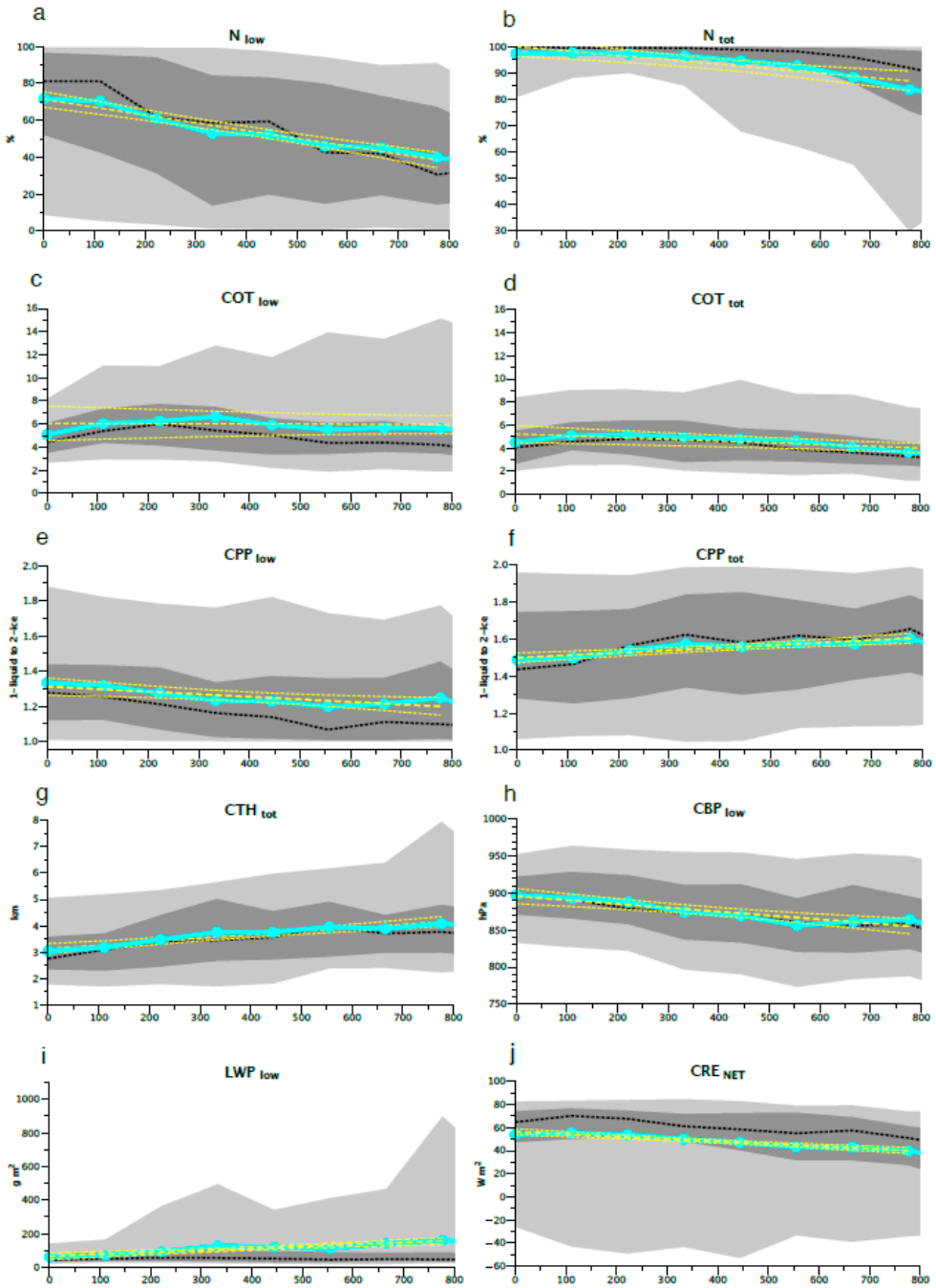

Figure 6. Changes in cloud characteristics along 38 °E from the sea ice margin (95% of sea ice concentration) for the analyzed sample of intense MCAOs: (**a**) the fraction of low-level clouds (%), (**b**) the fraction of total cloud cover (%), (**c**) the optical depth of low-level clouds; (**d**) the optical depth of total cloud cover; (**e**) the cloud particle phase of low-level clouds (where 1 is liquid and 2 is ice); (**f**) the cloud particle phase of total cloud cover (where 1 is liquid and 2 is ice); (**g**) the low-level cloud top height (km); (**h**) the low-level cloud base pressure (hPa); (**i**) the low-level cloud liquid water path (g m^{-2}); and (**j**) the net cloud radiative effect on the surface (W m^{-2}). Light grey areas show values in the 5th–95th percentile range, dark grey areas show values in the 25th–75th percentile range, and black dotted lines show the median value. Turquoise curves are averages over all selected MCAOs. Yellow dashed and small dotted lines show a linear trend with a 95% confidence interval.

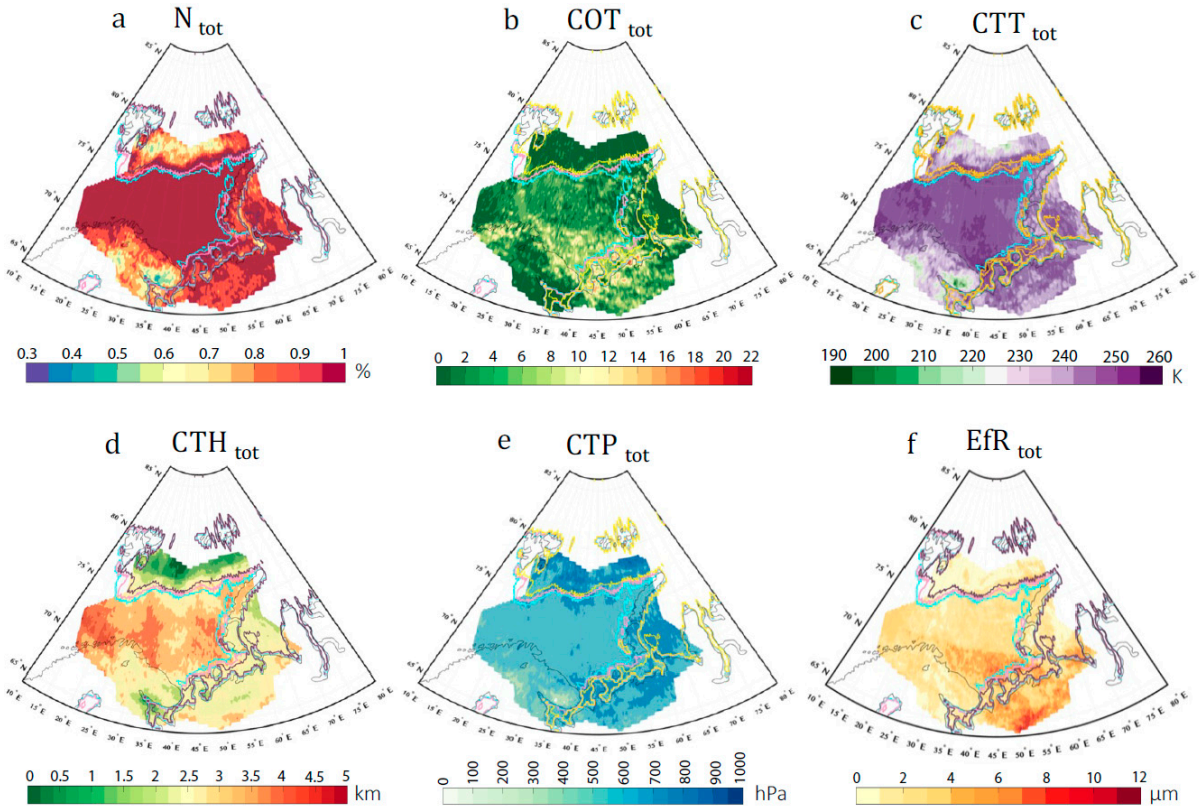

Figure 7. Cloud characteristics averaged for 19 MCAO events based on MODIS (Terra) data, for total cloud cover: (**a**) cloud fraction (%), (**b**) cloud optical thickness, (**c**) cloud top temperature (K), (**d**) cloud top height (km), (**e**) cloud top pressure (hPa), and (**f**) cloud droplet effective radius (µm). The lines represent the 25th, 50th, and 75th percentiles (turquoise, pink, and yellow lines, respectively) of the ice boundary (15% concentration), averaged for the sample of the 19 MCAO episodes.

We found that the sea surface is almost completely covered by clouds (95–100%), according to the data from both satellites, while over the ice and the continent, the number of clouds is significantly lower (Figure 7a). A decrease in the cloud fraction observed by CERES is not as pronounced in the MODIS data, presumably due to the fact that only total cloud cover information is available from the 5 min MODIS data. The overall southward increase in cloud optical thickness (Figure 7b) is pronounced, with a patchy structure observed that is related to the cloud distribution in the cellular convection. It is worth noting that the CERES data show a smaller southward increase in optical thickness. Further analysis is needed to determine whether this difference is physical or due to sampling differences.

In general, clouds become higher during the southward passage of the air mass (Figure 7d), gradually increasing from 1.5 km to ~5 km, reaching a maximum as the air mass approaches the continent. As the CTH increases, the cloud top temperature also increases rather than decreases (Figure 7c), with temperatures at the cloud top increasing from 200–220 K to 250–260 K. The rapid decrease in CTT as the air mass transitions towards the continent is remarkable, with values dropping by 20–40 K on average. According to the CERES data (not shown), there is also an increase in the water phase fraction in the southerly direction. MODIS data show this increase as an increase in the droplet effective radius (Figure 7f). The cloud top pressure gradually decreases from 1000 hPa over the sea ice to 400 hPa over the continents, according to Aqua (Figure S4e), and from 800–900 hPa over the sea ice to 600 hPa over the BS and further, to 300–400 hPa over the Kola Peninsula (Figure 7e). As a result, analysis of both MODIS and CERES satellite data shows that clouds become warmer and higher as the MCAO develops, with a gradual increase in the liquid fraction and an increase in the radius of the liquid droplets.

3.4. Dependence of MCAO Cloud Characteristics on the Environmental Conditions

Scenarios for MCAO development vary, with assumed environmental conditions influencing these scenarios [14,28]. Specifically, the warming effect of clouds is statistically positively correlated with increasing SST and expanding ice-free surface areas (Table 3). It is likely that during intense MCAOs, as the ice margin shifts northwards, the expanded open sea area contributes significantly to the increase in latent heat flux, which enhances the transport of liquid water vapor into the atmosphere. This results in an increase in the liquid water path in the upper atmospheric layers, as well as an increase in the cloud fraction, both N_{tot} and N_{low} (Table 3). A warmer surface and a higher moisture content in the air correspond to higher and more developed low-level clouds, but to a reduction in high and mid-level clouds and, consequently, to a decrease in the total cloud top height. This relationship is partially confirmed in the study by Ref. [64]. Clouds under such conditions are predominantly composed of liquid droplet particles, which explains the negative correlation coefficients with the cloud phase parameter (Table 3). Our analysis shows that a 1 degree SST increase leads to an increase in CRE_{LW} of 6.1 W m^{-2}, a 6.9% increase in the fraction of low-level clouds, and a 9.44 g m^{-2} increase in the total liquid water path. Additionally, a 100 km increase in the distance to the sea ice margin leads to a 2.43% increase in N_{low} and a 4.97 g m^{-2} increase in LWP_{low}. An increase of 1 kg m^{-2} in the IWV increases the low-level clouds liquid water path by 9.57 g/m^2, N_{low} by 9.76%, and CRE_{LW} by 3.97 W/m^2. Note that these are median values of the Theil–Sen slope estimators, while their 90% confidence intervals imply a wider range of dependence of cloud characteristics on background condition parameters (Table 3). Most of the analyzed cloud characteristics display a statistically significant relationship with changes in environmental conditions.

Table 3. Dependence of cloud characteristics on background parameters, including the Mann–Kendall rank correlation coefficients (MK) and the non-parametric Theil–Sen slope estimators (TS). The environmental parameters include the distance from the sea ice margin (km), the sea surface temperature of the BS (°C), and the integral vertical water vapor content of the intruding air mass (kg m^{-2}). Bold and italics indicate statistically significant values at the 95% and 90% levels, respectively. In brackets are the bootstrap-based 90% confidence intervals for each TS slope estimator.

Parameter	Units [1]	Distance to Ice Margin km		SST °C		IWV kg m^{-2}	
		MK	**TS * 10^2**	**MK**	**TS**	**MK**	**TS**
N_{tot}	%	−0.01	−0.03 [−0.37, 0.42]	**0.20**	1.66 [0.20, 2.91]	−0.11	−0.95 [−1.96, 0.12]
N_{low}	%	**0.19**	2.43 [0.55, 5.00]	**0.20**	6.90 [2.85, 11.94]	**0.21**	9.76 [3.68, 18.76]
CTH_{tot}	km	**−0.16**	−0.10 [−0.19, −0.03]	**−0.22**	−0.34 [−0.54, −0.15]	**−0.28**	−0.61 [−0.92, −0.28]
CTH_{low}	km	**0.20**	0.03 [0.01, 0.05]	***0.14***	0.07 [0.01, 0.14]	0.02	0.01 [−0.10, 0.08]
LWP_{tot}	g m^{-2}	**0.40**	5.40 [3.79, 7.55]	**0.23**	9.44 [3.16, 15.52]	**0.15**	9.06 [0.12, 16.51]
LWP_{low}	g m^{-2}	**0.37**	4.97 [3.25, 6.85]	**0.25**	8.99 [3.43, 13.56]	**0.19**	9.57 [1.56, 15.90]

Table 3. *Cont.*

Parameter	Units [1]	Distance to Ice Margin km		SST °C		IWV kg m^{-2}	
		MK	TS * 10^2	MK	TS	MK	TS
COT_{tot}	*	**0.30**	0.34 [0.23, 0.47]	**0.37**	1.05 [0.70, 1.39]	0.05	0.24 [−0.37, 0.79]
COT_{low}	*	**0.32**	0.34 [0.21, 0.51]	**0.35**	1.06 [0.65, 1.46]	0.04	0.18 [−0.34, 0.77]
CPP_{tot}	*	**−0.25**	−0.03 [−0.06, −0.02]	**−0.21**	−0.08 [−0.14, −0.03]	**−0.30**	−0.15 [−0.24, −0.08]
CPP_{low}	*	**−0.25**	−0.02 [−0.04, −0.01]	**−0.22**	−0.05 [−0.09, −0.03]	**−0.31**	−0.10 [−0.16, −0.06]
CBP_{low}	hPa	−0.10	−1.24 [−3.09, 0.42]	**−0.12**	−4.70 [−9.16, 1.18]	**−0.19**	−9.01 [−15.69, −2.37]
SRB_{LW}	W m^{-2}	0.03	0.16 [−0.93, 1.23]	***0.14***	2.57 [0.11, 4.99]	**0.36**	7.78 [4.74, 10.89]
CRE_{LW}	W m^{-2}	**0.27**	1.59 [0.72, 2.64]	**0.40**	6.10 [4.08, 8.31]	**0.20**	3.97 [2.12, 6.52]
SRB_{SW}	W m^{-2}	−0.06	0.00 [0.00, 0.00]	0.02	0.00 [0.00, 0.00]	0.04	0.00 [0.00, 0.00]
CRE_{SW}	W m^{-2}	**−0.23**	0.00 [0.00, 0.00]	−0.13	0.00 [0.00, 0.00]	−0.04	0.00 [0.00, 0.00]
SRB_{NET}	W m^{-2}	0.05	0.30 [−0.78, 1.24]	**0.17**	3.02 [0.79, 4.82]	**0.33**	7.72 [74.33, 11.33]
CRE_{NET}	W m^{-2}	**0.23**	1.58 [0.68, 2.80]	**0.33**	5.43 [3.26, 7.56]	**0.18**	3.94 [1.37, 6.52]

[1] Unitless variables are indicated by an asterisk (*).

4. Conclusions

A sample of intense MCAO cases over the Barents Sea is evaluated, with a focus on cloud characteristics. In total, 72 MCAOs were identified based on the M-index calculated from ERA-Interim data regarding surface temperature and potential temperature at the 800 hPa level for the period of 2000–2018. CERES and MODIS satellite data were used to evaluate the micro- and macrophysical parameters and the radiative properties of clouds within selected MCAOs. A significant increase in low-level clouds near the ice edge (up to +25% anomalies) and a smooth transition to upper-level clouds are revealed. The total cloud height during intense MCAOs is generally 500–700 m lower than that under neutral conditions. MCAOs induce a positive net cloud radiative effect, which peaks at +20 W m^{-2} (100 km from the ice edge) and gradually decreases towards the continent (–2.3 W m^{-2} per 100 km). We also evaluated the dependence of cloud characteristics on sea ice concentration and initial air mass properties using satellite data. We show that a 1°C increase in SST results in the CRE_{LW} rising by approximately ~6 W m^{-2}, the low-level cloudiness by ~7%, and the moisture content by 9.4 g/m^2. In turn, an increase in the passing distance for 100 km downwind of the sea ice margin leads to an increase in the N_{tot} of 2.4% and the LWP_{tot} of 5.4 g m^{-2}. An increase of 1 kg m^{-2} in the water vapor content of the initial air mass increases the LWP by 9.1 g m^{-2}, the N_{tot} by 9.8%, and the CRE_{LW} by 4.0 W m^{-2}.

Our results reveal the differences between the hourly adjusted CERES and the 5 min resolution MODIS satellite data. This highlights the limitations of our study. Although satellite and reanalysis data are often used for Arctic cloud and energy budget studies, biases in SW and LW radiation fields and many cloud characteristics are still present due to the presence of sea ice, temperature inversions, a high zenith angle, etc. [48,65]. This can be partly overcome by relying on the analysis of field experiments, such as COMBLE [66],

but such an approach fails to provide a large sample for analysis, and it must still be complemented by long-term data. Another limitation of our study is the use of outdated ERA-Interim reanalysis. In particular, the use of the more recent ERA5 reanalysis [67] allows for the extension of the period of the modern data and the increase in the sample size. This would likely not substantially change the results obtained for the satellite-based cloud characteristics of MCAOs, but it could make them more specific. Such an analysis should be carried out in future studies.

Fully understanding Marine cold air outbreaks remains challenging. For a thorough analysis of the internal processes occurring in MCAOs, a combination of in situ measurements is needed to represent the entire passage of an MCAO air mass. In addition to satellite or model data, a spectrum of in situ measurements, i.e., airborne, ground-based, and ocean-based instrument campaigns, is required, which is a challenging but necessary task. A broader survey is needed to fill the knowledge gap regarding the characteristics of MCAOs and their evolution in a changing climate, as well as and to avoid inconsistencies between all available data. Our study provides an important, but by no means conclusive, compilation of information to fill this gap, and this information can be used for comparison with in situ measurements and for the validation of cloud simulations in current climate and numerical weather prediction models.

Supplementary Materials: The following supporting information can be downloaded at: https://www.mdpi.com/article/10.3390/atmos15030317/s1, Figure S1: Same as for Figure 4, but for (a) the downward longwave radiation flux (W m^{-2}) and (b) the longwave cloud radiative effect (W m^{-2}); Figure S2: Same as for Figure 5, but for anomaly values of longwave surface radiation effect (W m^{-2}) for 72 intense MCAO events; Figure S3: Same as for Figure 6, but for (a) the low-level cloud liquid water path (g m^{-2}) of the total cloud cover and (b) the longwave cloud radiative effect on the surface (W m^{-2}); Figure S4: Same as for Figure 7, but for 14 MCAO events based on MODIS Aqua data.

Author Contributions: Conceptualization, A.C. and A.N.; methodology, A.C. and A.N.; data curation, A.C. and A.N.; validation, A.N.; visualization, A.N.; writing—original draft preparation, A.N.; writing—review and editing, A.C.; supervision, A.C.; project administration, A.C.; acquisition of funding, A.C. All authors have read and agreed to the published version of the manuscript.

Funding: This research was supported by the Russian Science Foundation (grant number 23-47-00104). The analysis of the MODIS data was supported by the state assignment of the A. M. Obukhov Institute of Atmospheric Physics RAS (FMWR-2022-0014).

Institutional Review Board Statement: Not applicable.

Informed Consent Statement: Not applicable.

Data Availability Statement: The data presented in this study are available on request from the corresponding author. The data are not publicly available due to PhD thesis restrictions. The surface analysis map in Figure 1a can be found in the NCEP archive of the German database in Ref. [35]. The satellite image in Figure 1b is from the Moderate Resolution Imaging Spectroradiometer (MODIS) onboard the Terra/Aqua satellite, provided by the National Aeronautics and Space Administration (NASA) via [36]. The cloud radiative properties can be retrieved from CERES (the Clouds and the Earth's Radiant Energy System) satellite data in Ref. [47]. Product data from MODIS (Moderate Resolution Imaging Spectroradiometer) on board the Terra and Aqua satellites (MOD06 and MYD06 products for Terra and Aqua, respectively) can be obtained from Ref. [54]. Satellite pass timing data can be retrieved using satellite imagery and orbital trajectories derived from NASA data [34,47]. The sea ice concentration dataset can be downloaded from the NSIDC (National Snow and Ice Data Center) in Ref. [37]. The ERA-Interim data are no longer available for public download but can be provided by the corresponding author upon request.

Acknowledgments: The authors appreciate the anonymous reviewers for their constructive and efficient comments regarding the manuscript. We especially would like to thank Alexander Timazhev for the technical assistance and Dmitry Chechin for his advice throughout the working process.

Conflicts of Interest: The authors declare no conflicts of interest.

Abbreviation

Abbreviation	Full Name	Unit
	Parameters	
Parameter	**Full name**	**Unit**
M-index	index representing MCAO intensity	K
$CRE_{LW/SW/NET}$	cloud radiative effect	W m^{-2}
$SRB_{LW/SW/NET}$	surface radiative budget	W m^{-2}
N	cloud fraction	%
COT	cloud optical thickness	units
CTH	cloud top height	km
LWP	liquid water path	g m^{-2}
CBP	cloud base pressure	hPa
CTP	cloud top pressure	hPa
CPP	cloud particle phase (1—liquid, 2—solid)	units
CTT	cloud top temperature	K
IWV	integral water vapor content	kg m^{-2}
EfR	cloud droplet effective radius	µm
Other		
CERES	Clouds and the Earth's Radiant Energy System	
MODIS	Moderate Resolution Imaging Spectroradiometer	
AM	air mass	
SIC	sea ice concentration	
ICE95	ice edge 95%	
ICE30	ice edge 30%	
CS	clear-sky conditions	
AS	all-sky conditions	
MK	Mann–Kendall correlation coefficients	
TS	Theil–Sen slope estimator	
SFC	surface	
BS	Barents Sea	

References

1. Wendisch, M.; Stapf, J.; Becker, S.; Ehrlich, A.; Jäkel, E.; Klingebiel, M.; Lüpkes, C.; Schäfer, M.; Shupe, M.D. Effects of variable ice–ocean surface properties and air mass transformation on the Arctic radiative energy budget. *Atmos. Chem. Phys.* **2023**, *23*, 9647–9667. [CrossRef]
2. Esau, I.; Pettersson, L.H.; Cancet, M.; Chapron, B.; Chernokulsky, A.; Donlon, C.; Sizov, A.; Soromotin, A.; Johannesen, J.A. The Arctic Amplification and Its Impact: A Synthesis through Satellite Observations. *Remote Sens.* **2023**, *15*, 1354. [CrossRef]
3. Serreze, M.C.; Barry, R.G. Processes and impacts of Arctic amplification: A research synthesis. *Glob. Planet. Change* **2011**, *77*, 85–96. [CrossRef]
4. Cohen, J.; Screen, J.A.; Furtado, J.C.; Barlow, M.; Whittleston, D.; Coumou, D.; Francis, J.; Dethloff, K.; Entekhabi, D.; Overland, J.; et al. Recent Arctic amplification and extreme mid-latitude weather. *Nat. Geosci.* **2014**, *7*, 627–637. [CrossRef]
5. Vavrus, S.; Walsh, J.E.; Chapman, W.L.; Portis, D. The behavior of extreme cold air outbreaks under greenhouse warming. *Int. J. Climatol.* **2006**, *26*, 1133–1147. [CrossRef]
6. Chernokulsky, A.; Esau, I. Cloud cover and cloud types in the Eurasian Arctic in 1936–2012. *Int. J. Climatol.* **2019**, *39*, 5771–5790. [CrossRef]
7. Francis, J.A.; Hunter, E. New insight into the disappearing Arctic sea ice. *EOS Trans. Am. Geophys. Union* **2006**, *87*, 509–511. [CrossRef]
8. Graversen, R.G.; Wang, M. Polar amplification in a coupled climate model with locked albedo. *Clim. Dyn.* **2009**, *33*, 629–643. [CrossRef]
9. Kolstad, E.W.; Bracegirdle, T.J. Marine cold-air outbreaks in the future: An assessment of IPCC AR4 model results for the Northern Hemisphere. *Clim. Dyn.* **2008**, *30*, 871–885. [CrossRef]
10. Narizhnaya, A.I.; Chernokulsky, A.V.; Akperov, M.G.; Chechin, D.G.; Esau, I.; Timazhev, A.V. Marine cold air outbreaks in the Russian Arctic: Climatology, interannual variability, dependence on sea-ice concentration. *IOP Conf. Ser. Earth Environ. Sci.* **2020**, *606*, 012039. [CrossRef]
11. Papritz, L.; Hauswirth, D.; Hartmuth, K. Moisture origin, transport pathways, and driving processes of intense wintertime moisture transport into the Arctic. *Weather Clim. Dyn.* **2022**, *3*, 1–20. [CrossRef]

12. Brümmer, B. Boundary-layer modification in wintertime cold-air outbreaks from the Arctic sea ice. *Bound. Layer Meteorol.* **1996**, *80*, 109–125. [CrossRef]
13. Pithan, F.; Svensson, G.; Caballero, R.; Chechin, D.; Cronin, T.W.; Ekman, A.M.; Neggers, R.; Shupe, M.D.; Solomon, A.; Tjernström, M.; et al. Role of air-mass transformations in exchange between the Arctic and mid-latitudes. *Nat. Geosci.* **2018**, *11*, 805–812. [CrossRef]
14. McCoy, I.L.; Wood, R.; Fletcher, J.K. Identifying meteorological controls on open and closed mesoscale cellular convection associated with marine cold air outbreaks. *J. Geophys. Res. Atmos.* **2017**, *122*, 11678–11702. [CrossRef]
15. Brümmer, B. Roll and cell convection in wintertime Arctic cold-air outbreaks. *J. Atmos. Sci.* **1999**, *56*, 2613–2636. [CrossRef]
16. Kolstad, E.W.; Bracegirdle, T.J.; Seierstad, I.A. Marine cold-air outbreaks in the North Atlantic: Temporal distribution and associations with large-scale atmospheric circulation. *Clim. Dyn.* **2009**, *33*, 187–197. [CrossRef]
17. Papritz, L.; Pfahl, S.; Sodemann, H.; Wernli, H. A climatology of cold air outbreaks and their impact on air–sea heat fluxes in the high-latitude South Pacific. *J. Clim.* **2015**, *28*, 342–364. [CrossRef]
18. Papritz, L.; Spengler, T. A Lagrangian climatology of wintertime cold air outbreaks in the Irminger and Nordic Seas and their role in shaping air–sea heat fluxes. *J. Clim.* **2017**, *30*, 2717–2737. [CrossRef]
19. Kolstad, E.W. Higher ocean wind speeds during marine cold air outbreaks. *Q. J. R. Meteorol. Soc.* **2017**, *143*, 2084–2092. [CrossRef]
20. Terpstra, A.; Renfrew, I.A.; Sergeev, D.E. Characteristics of cold-air outbreak events and associated polar mesoscale cyclogenesis over the North Atlantic region. *J. Clim.* **2021**, *34*, 4567–4584. [CrossRef]
21. Fletcher, J.K.; Mason, S.; Jakob, C. A climatology of clouds in marine cold air outbreaks in both hemispheres. *J. Clim.* **2016**, *29*, 6677–6692. [CrossRef]
22. Mokhov, I.I.; Chernokul'Skii, A.V.; Akperov, M.G.; Dufresne, J.L.; Le Treut, H. Variations in the characteristics of cyclonic activity and cloudiness in the atmosphere of extratropical latitudes of the Northern Hemisphere based from model calculations compared with the data of the reanalysis and satellite data. *Dokl. Earth Sci.* **2009**, *424*, 147. [CrossRef]
23. Pichugin, M.K.; Mitnik, L.M. Cold invasions over the Bering Sea: Satellite multisensor analysis. *Mod. Probl. Remote Sens. Earth Space* **2009**, *6*, 172–179. (In Russian) [CrossRef]
24. Myslenkov, S.; Shestakova, A.; Chechin, D. The impact of sea waves on turbulent heat fluxes in the Barents Sea according to numerical modeling. *Atmos. Chem. Phys.* **2021**, *21*, 5575–5595. [CrossRef]
25. Chechin, D.G.; Pichugin, M.K. Cold-air outbreaks over the ocean at high latitudes and associated mesoscale atmospheric circulations: Problems of numerical modelling. *Izv. Atmos. Ocean. Phys.* **2015**, *51*, 1034–1050. [CrossRef]
26. Dahlke, S.; Solbès, A.; Maturilli, M. Cold air outbreaks in Fram Strait: Climatology, trends, and observations during an extreme season in 2020. *J. Geophys. Res. Atmos.* **2022**, *127*, e2021JD035741. [CrossRef]
27. Ezau, I.N.; Chernokulsky, A.V. Convective cloud fields in the Atlantic sector of the Arctic: Satellite and ground observations. *Earth Explor. Space* **2015**, *2*, 49. (In Russian) [CrossRef]
28. Tornow, F.; Ackerman, A.S.; Fridlind, A.M. Preconditioning of overcast-to-broken cloud transitions by riming in marine cold air outbreaks. *Atmos. Chem. Phys.* **2021**, *21*, 12049–12067. [CrossRef]
29. Abel, S.J.; Boutle, I.A.; Waite, K.; Fox, S.; Brown, P.R.; Cotton, R.; Lloyd, G.; Choularton, T.W.; Bower, K.N. The role of precipitation in controlling the transition from stratocumulus to cumulus clouds in a Northern Hemisphere cold-air outbreak. *J. Atmos. Sci.* **2017**, *74*, 2293–2314. [CrossRef]
30. Field, P.R.; Cotton, R.J.; McBeath, K.; Lock, A.P.; Webster, S.; Allan, R.P. Improving a convection-permitting model simulation of a cold air outbreak. *Q. J. R. Meteorol. Soc.* **2014**, *140*, 124–138. [CrossRef]
31. Murray-Watson, R.J.; Gryspeerdt, E.; Goren, T. Investigating the development of clouds within marine cold-air outbreaks. *Atmos. Chem. Phys.* **2023**, *23*, 9365–9383. [CrossRef]
32. Mateling, M.E.; Pettersen, C.; Kuli3e, M.S.; L'Ecuyer, T.S. Marine Cold-Air Outbreak Snowfall in the North Atlantic: A CloudSat Perspective. *J. Geophys. Res. Atmos.* **2023**, *128*, e2022JD038053. [CrossRef]
33. Wu, P.; Ovchinnikov, M. Cloud Morphology Evolution in Arctic Cold-Air Outbreak: Two Cases During COMBLE Period. *J. Geophys. Res. Atmos.* **2022**, *127*, e2021JD035966. [CrossRef]
34. Petoukhov, V.; Semenov, V.A. A link between reduced Barents-Kara sea ice and cold winter extremes over northern continents. *J. Geophys. Res. Atmos.* **2010**, *115*, D21. [CrossRef]
35. Website of the German Meteorological Office. Available online: https://wetterzentrale.de (accessed on 23 September 2020).
36. EOSDIS Worldview. Available online: https://worldview.earthdata.nasa.gov (accessed on 7 February 2022).
37. NSIDC Archive. Available online: https://nsidc.org/data/data-programs/nsidc-daac (accessed on 7 September 2019).
38. Comiso, J.C. *Bootstrap Sea Ice Concentrations from Nimbus-7 SMMR and DMSP SSM/I-SSMIS, Version 3 [Data Set]*; NASA National Snow and Ice Data Center Distributed Active Archive Center: Boulder, CO, USA, 2017. [CrossRef]
39. Dee, D.P.; Uppala, S.M.; Simmons, A.J.; Berrisford, P.; Poli, P.; Kobayashi, S.; Andrae, U.; Balmaseda, M.A.; Balsamo, G.; Bauer, P.; et al. The ERA-Interim reanalysis: Configuration and performance of the data assimilation system. *Q. J. R. Meteorol. Soc.* **2011**, *137*, 553–597. [CrossRef]
40. Polkova, I.; Afargan-Gerstman, H.; Domeisen, D.I.; King, M.P.; Ruggieri, P.; Athanasiadis, P.; Baehr, J. Predictors and prediction skill for marine cold-air outbreaks over the Barents Sea. *Q. J. R. Meteorol. Soc.* **2021**, *147*, 2638–2656. [CrossRef]
41. Yu, Y.; Cai, M.; Ren, R.; Rao, J. A closer look at the relationships between meridional mass circulation pulses in the stratosphere and cold air outbreak patterns in northern hemispheric winter. *Clim. Dyn.* **2018**, *51*, 3125–3143. [CrossRef]

42. Lindsay, R.; Wensnahan, M.; Schweiger, A.; Zhang, J. Evaluation of seven different atmospheric reanalysis products in the Arctic. *J. Clim.* **2014**, *27*, 2588–2606. [CrossRef]
43. Wielicki, B.A.; Barkstrom, B.R.; Baum, B.A.; Charlock, T.P.; Green, R.N.; Kratz, D.P.; Welch, R.M. Clouds and the Earth's Radiant Energy System (CERES): Algorithm overview. *IEEE Trans. Geosci. Remote Sens.* **1998**, *36*, 1127–1141. [CrossRef]
44. Loeb, N.G.; Su, W.; Doelling, D.R.; Wong, T.; Minnis, P.; Thomas, S.; Miller, W.F. Earth's top-of-atmosphere radiation budget. *Compr. Remote Sens.* **2018**, *5*, 67–84. [CrossRef]
45. Doelling, D.; Haney, C.; Bhatt, R.; Scarino, B.; Gopalan, A. Geostationary enhanced temporal interpolation for CERES flux products. *J. Atmos. Ocean. Technol.* **2013**, *30*, 1072–1090. [CrossRef]
46. Minnis, P.; Sun-Mack, S.; Young, D.F.; Heck, P.W.; Garber, D.P.; Chen, Y.; Yang, P. CERES edition-2 cloud property retrievals using TRMM VIRS and Terra and Aqua MODIS data—Part I: Algorithms. *IEEE Trans. Geosci. Remote Sens.* **2011**, *49*, 4374–4400. [CrossRef]
47. CERES Archive. Available online: https://ceres.larc.nasa.gov (accessed on 20 December 2019).
48. Di Biagio, C.; Pelon, J.; Blanchard, Y.; Loyer, L.; Hudson, S.R.; Walden, V.P.; Granskog, M.A. Toward a Better Surface Radiation Budget Analysis Over Sea Ice in the High Arctic Ocean: A Comparative Study Between Satellite, Reanalysis, and local-scale Observations. *J. Geophys. Res. Atmos.* **2021**, *126*, e2020JD032555. [CrossRef]
49. Riihelä, A.; Devasthale, A.; Karlsson, K.G.; Thomas, M. An intercomparison and validation of satellite-based surface radiative energy flux estimates over the Arctic. *J. Geophys. Res. Atmos.* **2017**, *122*, 4829–4848. [CrossRef]
50. Ramanathan, V.; Cess, R.D.; Harrison, E.F.; Minnis, P.; Barkstrom, B.R.; Ahmad, E.; Hartmann, D. Cloud-radiative forcing and climate: Results from the Earth Radiation Budget Experiment. *Science* **1989**, *243*, 57–63. [CrossRef] [PubMed]
51. Trepte, Q.Z.; Minnis, P.; Sun-Mack, S.; Yost, C.R.; Chen, Y.; Jin, Z.; Chee, T.L. Global cloud detection for CERES Edition 4 using Terra and Aqua MODIS data. *IEEE Trans. Geosci. Remote Sens.* **2019**, *57*, 9410–9449. [CrossRef]
52. Huang, Y.; Dong, X.; Kay, J.E.; Xi, B.; McIlhattan, E.A. Toward a more realistic representation of surface albedo in NASA CERES-derived surface radiative fluxes. *Elementa* **2022**, *10*, 00013. [CrossRef]
53. Platnick, S.; Meyer, K.G.; King, M.D.; Wind, G.; Amarasinghe, N.; Marchant, B.; Riedi, J. The MODIS cloud optical and microphysical products: Collection 6 updates and examples from Terra and Aqua. *IEEE Trans. Geosci. Remote Sens.* **2016**, *55*, 502–525. [CrossRef]
54. Moderate Resolution Imaging Spectroradiometer (MODIS). Available online: https://lance.modaps.eosdis.nasa.gov/modis/ (accessed on 7 February 2022).
55. Kolstad, E.W.; Breiteig, T.; Scaife, A.A. The association between stratospheric weak polar vortex events and cold air outbreaks in the Northern Hemisphere. *Q. J. R. Meteorol. Soc.* **2010**, *136*, 886–893. [CrossRef]
56. Fletcher, J.; Mason, S.; Jakob, C. The climatology, meteorology, and boundary layer structure of marine cold air outbreaks in both hemispheres. *J. Clim.* **2016**, *29*, 1999–2014. [CrossRef]
57. Allan, R.P. Combining satellite data and models to estimate cloud radiative effect at the surface and in the atmosphere. *Meteorol. Appl.* **2011**, *18*, 324–333. [CrossRef]
58. Becker, S.; Ehrlich, A.; Schäfer, M.; Wendisch, M. Airborne observations of the surface cloud radiative effect during different seasons over sea ice and open ocean in the Fram Strait. *Atmos. Chem. Phys.* **2023**, *23*, 7015–7031. [CrossRef]
59. Barrientos-Velasco, C.; Deneke, H.; Hünerbein, A.; Griesche, H.J.; Seifert, P.; Macke, A. Radiative closure and cloud effects on the radiation budget based on satellite and shipborne observations during the Arctic summer research cruise, PS106. *Atmos. Chem. Phys.* **2022**, *22*, 9313–9348. [CrossRef]
60. Oreopoulos, L.; Rossow, W.B. The cloud radiative effects of International Satellite Cloud Climatology Project weather states. *J. Geophys. Res. Atmos.* **2011**, *116*, D10. [CrossRef]
61. Wilks, D.S. *Statistical Methods in the Atmospheric Sciences*; Academic Press: Cambridge, MA, USA, 2011; Volume 100. [CrossRef]
62. Cronin, T.W.; Tziperman, E. Low clouds suppress Arctic air formation and amplify high-latitude continental winter warming. *Proc. Natl. Acad. Sci. USA* **2015**, *112*, 11490–11495. [CrossRef] [PubMed]
63. Kay, J.E.; L'Ecuyer, T. Observational constraints on Arctic Ocean clouds and radiative fluxes during the early 21st century. *J. Geophys. Res. Atmos.* **2013**, *118*, 7219–7236. [CrossRef]
64. Ruiz-Donoso, E.; Ehrlich, A.; Schäfer, M.; Jäkel, E.; Schemann, V.; Crewell, S.; Wendisch, M. Small-scale structure of thermodynamic phase in Arctic mixed-phase clouds observed by airborne remote sensing during a cold air outbreak and a warm air advection event. *Atmos. Chem. Phys.* **2020**, *20*, 5487–5511. [CrossRef]
65. Graham, R.M.; Cohen, L.; Ritzhaupt, N.; Segger, B.; Graversen, R.G.; Rinke, A.; Walden, V.P.; Granskog, M.A.; Hudson, S.R. Evaluation of six atmospheric reanalyses over Arctic sea ice from winter to early summer. *J. Clim.* **2019**, *32*, 4121–4143. [CrossRef]
66. Geerts, B.; Giangrande, S.E.; McFarquhar, G.M.; Xue, L.; Abel, S.J.; Comstock, J.M.; Wu, P. The COMBLE campaign: A study of marine boundary layer clouds in Arctic cold-air outbreaks. *Bull. Am. Meteorol. Soc.* **2022**, *103*, E1371–E1389. [CrossRef]
67. Hersbach, H.; Bell, B.; Berrisford, P.; Hirahara, S.; Horányi, A.; Muñoz-Sabater, J.; Thépaut, J.N. The ERA5 global reanalysis. *Q. J. R. Meteorol. Soc.* **2020**, *146*, 1999–2049. [CrossRef]